Title
Plasticity-induced damage and material loss in oscillatory contacts

Authors
Cen, Jialiang
Komvopoulos, Kyriakos

Publication Date
2022-11-01

DOI
10.1016/j.ijsolstr.2022.111932

Peer reviewed

International Journal of Solids and Structures 254–255 (2022) 111932

Contents lists available at ScienceDirect

International Journal of Solids and Structures

journal homepage: www.elsevier.com/locate/ijsolstr

Plasticity-induced damage and material loss in oscillatory contacts

Jialiang Cen, Kyriakos Komvopoulos *

Department of Mechanical Engineering, University of California, Berkeley, CA 94720, USA

ARTICLE INFO

Keywords:
Damage
Finite element method
Friction
Loss of material
Plasticity
Oscillatory contacts
Wear

ABSTRACT

Knowledge of plasticity-induced damage leading to the loss of material in oscillatory contacts is of paramount importance to various electromechanical systems comprising contact-mode elements exposed to high-frequency vibrations. However, experimental investigation of the wear behavior of devices experiencing microscopic oscillatory contact (fretting) is complex, time consuming, and expensive. More importantly, the progression of critical damage processes, such as the decrease of the material's strength with the accumulation of plastic deformation in the vicinity of the contact interface and the removal of material in the form of microscopic wear debris, cannot be tracked in real time, necessitating cumbersome and costly post-testing microanalysis. Alternatively, computational wear modeling is more effective than experiments and can provide valuable insight into the effect of important parameters, such as load, coefficient of friction, oscillation amplitude, and material behavior, on the loss of material during oscillatory sliding contact. Accordingly, the principal objective of this study was to introduce a computational approach, which can be used to analyze the loss of material due to plasticity-induced damage in oscillatory mechanical components. To achieve this aim, a plane-strain finite element model of a rigid cylinder in reciprocating sliding contact with an elastic-plastic half-space exhibiting isotropic strain hardening was used to study how the evolution of damage due to the progression of plasticity leads to the loss of material. A quasi-static, isothermal damage model based on a ductile failure criterion was implemented in the finite element analysis to simulate the removal of the fully damaged elements. Numerical results illuminate the effects of the load and coefficient of friction on the development of plasticity, cumulative damage, and loss of material with accruing oscillation cycles. The deviation of the wear behavior from classical wear theory in the high-load simulations is explained by the plastic shear strain distribution and less slip at the contact interface encountered at high loads. The novelty of this study is the development of a computational methodology, which sheds light into the evolution of plasticity, damage, and loss of material in reciprocating sliding contacts and provides an effective computational capability for assessing the effects of load, friction, and material behavior on the mechanical performance of components operating in oscillatory contact mode.

1. Introduction

Oscillatory sliding contact affects the performance and longevity of a wide range of contact-mode electromechanical systems, contributing to frictional energy dissipation and the removal of material in the form of fine wear debris. The primitive studies of Cattaneo (1938) and Mindlin (1949) illuminated the effect of normal and tangential (shear) traction at the contact interface of two elastic bodies on the inception of slip and the deviation of the deformation response from that predicted by the classical contact theory of Hertz (1882). Mindlin and Deresiewicz (1953) investigated the contact behavior of two identical elastic spheres and reported an increase of the tangential force Q with increasing lateral displacement under a constant load P in conjunction with the development of a circular stick zone at the center of the contact region surrounded by an annulus slip zone. The stick zone shrunk with the increase of the tangential force and ultimately vanished when $Q = \mu P$, where μ is the coefficient of friction. When the preceding slip condition was satisfied, the tangential force remained constant and full slip initiated at the contact interface. These early studies provided the incentive to examine the instigation of stick and slip under various contact conditions. For instance, Björklund (1997) investigated elastic contact of a rough surface with a perfectly flat surface under both normal and tangential loadings and observed a dependence of micro-slip at the contact interface on the standard deviation of the asperity heights. Jäger (1998) obtained analytical solutions of the tangential traction and displacements in an elastic half-space subjected to quasi-static normal and

* Corresponding author.
E-mail address: kyriakos@me.berkeley.edu (K. Komvopoulos).

https://doi.org/10.1016/j.ijsolstr.2022.111932
Received 7 June 2022; Received in revised form 8 August 2022; Accepted 10 August 2022
Available online 13 August 2022

tangential loadings. Block and Keer (2008) used the summation of evenly spaced Flamant solutions to analyze periodic contact under various interfacial conditions, such as complete stick, partial slip, and frictionless sliding. Goryachev et al. (2012) examined two-dimensional elastic contact between a flat half-space and a patterned half-space with periodically arranged grooves of variable height and identical material properties. It was shown that when the slip condition $\tau = \mu\, p$ (where τ and p are the nominal shear stress and contact pressure, respectively) was satisfied, the edges of the slip zones reached the groove edges, causing a transition from partial slip at the boundaries to global slip of the bodies, with the wider grooves augmenting the growth of the slip zone with the increase of the tangential force. Klimchuk and Ostryk (2020) investigated the two-dimensional Cattaneo–Mindlin elastic contact problem of two identical cylindrical bodies and obtained analytical results of the stresses inside the bodies and the contact interface and elucidated the effect of friction on the distribution of the maximum tangential stress and the development of an adhesive region at the contact interface.

Despite important insight into the mechanics of oscillatory contacts derived from the previous studies, analyzing the material removal process in oscillatory contacts requires computational methods that account for the effect of various inelastic deformation processes on cumulative damage. For instance, Kuno et al. (1989) investigated both analytically and experimentally the effect of crack initiation and propagation on fretting fatigue. Fouvry et al. (1996) used an elastic Hertzian-Mindlin contact description to quantify damage and observed wear debris formation under gross slip conditions. Giannakopoulos and Suresh (1998) used a three-dimensional finite element model of a sphere in oscillatory contact with a flat surface of the same material to study the effects of partial slip, interfacial friction, and externally applied mean stress on the evolution of deformation and damage. Ambrico and Begley (2000) used a plane-strain model of a rigid cylinder cyclically loaded onto a flat elastic-plastic substrate to examine the progression of plasticity in the substrate during fretting and obtained numerical results that illuminate the development of plasticity, shakedown, and ratcheting in the substrate in terms of the coefficient of friction and the cyclically applied tangential force. Etsion (2010) argued that the assumptions made in the classical Cattaneo-Mindlin problem may not be physical and proposed an alternative approach for solving this problem in which the inception of sliding is treated as a plastic failure mode. Eriten et al. (2011) used Mindlin's partial slip response to monotonic and cyclic loading and incorporated elastic-plastic preload and preload-dependent friction coefficient models to predict the tangential response of the spherical asperity contacts between nominally flat surfaces undergoing fretting in terms of geometric and material properties. Song and Komvopoulos (2014) used a modified Mindlin theory to model stick-slip at the asperity contacts between a rigid fractal surface in oscillatory contact with an elastic-plastic half-space, considering the contributions of adhesion and plowing friction mechanisms to the friction force. Chen and Etsion (2019) used the finite element method (FEM) to investigate the inception of sliding at the contact interface of a coated elastic-plastic sphere strongly adhered to a rigid plane and obtained numerical results that explain the effect of the hard coating thickness on the static coefficient of friction.

Cumulative plasticity is a precursor to the loss of material in oscillatory contacts. Archard (1953) introduced the concept of the real area of contact for nominally flat surfaces and proposed an empirical law of adhesive wear in which the wear rate varies linearly with the load and is independent of the apparent area of contact. Atomistic simulations of wear particle formation at the asperity level performed by Aghababaei et al. (2017) showed a dependence of the volume of wear debris on the asperity junction size, consistent with Archard's postulated dependence of the adhesive wear volume on the real area of contact; however, the former atomistic simulations did not reveal a correlation between the volume of wear debris and the applied load. Frérot et al. (2018) provided two physics-based interpretations of the wear coefficient used in Archard's wear equation. Dimaki et al. (2020) used the discrete element method to study the effects of adhesion, yield stress, and shear strength on the modes of asperity deformation and fracture in adhesive wear. Salib et al. (2008) presented a FEM model of an elastic-plastic sphere fully adhered to a rigid flat plate and approximated the volume of a wear particle formed at the inception of sliding by assuming particle detachment along a slip path of maximum shear strain within the plastic zone; however, large discrepancies were found between predicted and experimental values of the wear coefficient. Pereira et al. (2017) used a statistical analysis that combines a microscale roughness model with a macroscale fretting wear model to explore the evolution of fretting wear. Yue and Abdel Wahab (2017) used an energy-based FEM model to obtain estimates of the wear scar and the wear volume under conditions of partial slip and gross sliding, constant and variable coefficient of friction, and fixed load. Wang et al. (2020) combined FEM modeling with a model reduction method to study the role of the slip amplitude, load, and oscillation cycles in fretting wear. Zhang and Etsion (2021) incorporated a ductile fracture criterion in a FEM model of an elastic-plastic, full-stick, spherical contact subjected to normal and tangential loadings and simulated the removal of material due to adhesive wear by eliminating those elements that satisfied the failure criterion, assuming wear particle formation due to cracking below the contact interface.

Damage models have been extensively used in numerical analyses to predict the removal of material. For instance, Ben Tkaya et al. (2007) explored the effect of the attack angle on the scratch behavior of isotropic and kinematic strain hardening materials and simulated damage initiation at a specified equivalent plastic strain and material removal due to the evolution of damage, depending on energy dissipation. Elwasli et al. (2015) incorporated the constitutive model of Johnson and Cook (1985) in an FEM model and analyzed the removal of material by scratching. Lou et al. (2014) proposed a damage model based on a ductile fracture criterion, which accounts for compressive and tensile stress triaxiality states. Mostaani et al. (2015) used FEM simulations of the scratching process to evaluate the effectiveness of the previous damage models to capture various deformation modes, e.g., plowing, wedge formation, and cutting.

Motivated by the foregoing studies and other recent efforts to model the removal of material in oscillatory contacts, a plane-strain FEM model of a rigid cylinder in reciprocating sliding contact with an elastic-plastic, strain hardening half-space was developed to examine the loss of material with the progression of plasticity-induced damage. A principal objective was to introduce a computational methodology, which can elucidate the effects of load, friction, oscillation cycles, and material behavior on the evolution of plasticity resulting in cumulative damage and ultimately the loss of material. The non-monotonic wear behavior encountered over a wide load range is interpreted in terms of the plastic shear strain distribution and the initiation of slip at the contact interface. Numerical results illuminate the effects of the applied load, plastic shear strain, and interfacial slip on the removal of material. An important contribution of the present study is the development of a computational framework for examining the effects of other important parameters (e.g., strain rate, oscillation amplitude, and frictional heating) on the evolution of damage leading to the loss of material in mechanical systems with elements operating in reciprocating sliding contact mode.

2. Modeling approach

2.1. Finite element mesh

The plane-strain problem examined in this study is schematically depicted in Fig. 1(a). A rigid cylinder of radius R is pressed against an elastic-plastic half-space under a normal load P and is then oscillated in the horizontal direction. The oscillation amplitude and the penetration depth are denoted by δ and d, respectively. The half-space is discretized by a $60R \times 60R$ finite element mesh consisting of 79,613 four-node, reduced-integration, quadrilateral elements with a total of 79,936

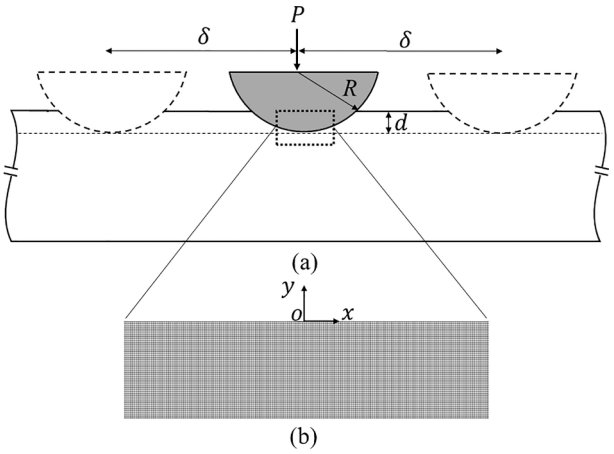

Fig. 1. (a) Cross-sectional schematic of a rigid cylinder loaded against a half-space and (b) refined finite element mesh at the near-surface region of the half-space.

nodes. To accurately capture the large strain gradients in the region where penetration and oscillation of the rigid cylinder takes place and to reduce the computation time, the FEM mesh is compartmentalized in three segments centered at point O, which is where the cylinder first contacts the half-space surface (Fig. 1(b)). The $0.4R \times 2R$ near-surface region of the mesh is uniformly refined with $0.004R$ size elements, as shown in Fig. 1(b), representing ~63% of the total number of elements. Outside of this region, a $1.2R \times 4R$ region is meshed with elements of gradually increasing size from $0.004R$ to $0.4R$. Finally, the outer part of the mesh is uniformly meshed with $0.4R$ size elements. The displacements of the nodes at the bottom boundary of the mesh are constrained in both x- and y-directions, whereas the nodes at the left and right boundaries of the mesh are free. Preliminary simulations confirmed that the above model dimensions, mesh refinement, and boundary conditions do not affect the magnitudes of global parameters (e.g., penetration depth). An oscillation cycle comprises four consecutive simulation steps of incrementally increasing x-displacement of the cylinder up to the specified oscillation amplitude, i.e., incremental lateral sliding of the cylinder in the distance ranges $[0, \delta]$, $[\delta, 0]$, $[0, -\delta]$, and $[-\delta, 0]$. In each simulation, the number of oscillation cycles N was sequentially increased to 10, while the load was fixed throughout the simulation.

Surface contact was simulated with a finite sliding algorithm, which treats the surfaces of the deformable half-space and the rigid cylinder as slave and master surfaces, respectively, and controls the relative separation and slip between the interacting surfaces. Each slave node coming into contact with the master surface is constrained to slide against the master surface, while the position of the slave node relative to the master surface is continuously tracked by the algorithm during the deformation. The finite sliding algorithm was implemented in the FEM analysis by using automatically generated contact elements. At each integration point of a contact element, the overclosure was adjusted to prevent a surface point of the deformed half-space from penetrating the surface of the rigid cylinder and the relative shear slip was computed afterwards. Coulomb friction was modeled by assigning to the contact elements a coefficient of friction, which relates the maximum allowable shear stress at the contact interface to the local contact pressure. Table 1 gives the geometric parameters, oscillation amplitude, and coefficient of friction used in the FEM simulations.

2.2. Damage and degradation model

The accumulation of plastic deformation due to the repetitive oscillation of the rigid cylinder under the applied load leads to cumulative damage, eventually resulting in the removal of the fully damaged elements. The evolution of cumulative damage in an isotropic strain

Table 1
Input parameters of the FEM simulations.

Parameter	Magnitude
Cylinder radius, R (mm)	5
Half-space height (mm)	300
Half-space width (mm)	300
Refined mesh height (mm)	2
Refined mesh width (mm)	10
Refined mesh size (mm)	0.02
Oscillation amplitude, δ (mm)	0.5
Coefficient of friction, μ	0.1, 0.3, 0.5

hardening material is depicted in the effective stress $\bar{\sigma}$ versus equivalent strain $\bar{\varepsilon}$ plot shown in Fig. 2. The stress-strain response comprises three characteristic deformation regions, namely elastic, strain hardening, and material degradation. Initially the material exhibits a linear elastic behavior up to the initial yield strength Y_0 (point A), beyond which the increase of stress causes the development of plastic deformation. In the absence of plasticity-induced damage leading to material degradation, the stress increases monotonically due to strain hardening (dashed curve in Fig. 2). However, a different response is encountered when the evolution of plasticity is accompanied by cumulative damage, quantified by the dimensionless damage variable ω $(0 \le \omega \le 1)$ given by

$$\omega = \int \frac{d\bar{\varepsilon}^p}{\bar{\varepsilon}_i^p} \tag{1}$$

where $\bar{\varepsilon}^p$ is the equivalent plastic strain and $\bar{\varepsilon}_i^p$ is the equivalent plastic strain at $\omega = 1$ (point B). Material degradation manifests itself in the form of a continuous decrease in yield stress and stiffness, controlled by the degradation parameter D $(0 \le D \le 1)$. Full material degradation (failure) is attained when the equivalent plastic strain at failure $\bar{\varepsilon}_f^p$ is reached (point C). A gradual material degradation process is modeled to avoid the instantaneous removal of the fully damaged elements ($\omega = 1$), which can generate artificial stress waves and dynamic effects.

A failure criterion is needed to model damage accumulation (path AB) and material degradation (path BC) of the plastically deformed elements. A common failure criterion for materials demonstrating significant ductility is that proposed by Johnson and Cook (1985), which for quasi-static, isothermal, strain hardening deformation takes the form,

$$\bar{\varepsilon}_i^p = A + Be^{C\eta} \tag{2}$$

where A, B, and C are material damage constants and η is a triaxiality parameter, given by $\eta = \sigma_m/\bar{\sigma}_M$, where σ_m is the hydrostatic stress and $\bar{\sigma}_M$ is the von Mises effective stress. Table 2 gives the material properties and the damage constants used in the FEM simulations. The mechanical properties given in Table 2 are typical of A2024-T351 aluminum alloy, which is widely used in aerospace, automotive, machining, and other industrial applications mainly due to its high strength, low weight, good machinability, and good fatigue resistance (Asad et al., 2014).

To ensure a smooth transition from the fully damaged state (point B) to the failure state (point C), an approach based on the fracture energy

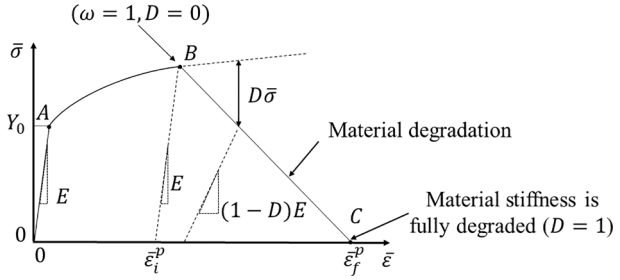

Fig. 2. Effective stress $\bar{\sigma}$ versus equivalent strain $\bar{\varepsilon}$ plot illustrating the evolution of material damage and degradation during deformation.

Table 2
Material properties and damage parameters used in the FEM simulations.

Parameter	Magnitude
Density, ρ (kg/m^3)	2700[(a)]
Initial yield strength, Y_0 (MPa)	352[(a)]
Elastic modulus, E (GPa)	73[(a)]
Poisson's ratio, ν	0.33[(a)]
Fracture energy, G_f (N/mm)	20[(a)]
Damage parameter, A	0.13[(b)]
Damage parameter, B	0.13[(b)]
Damage parameter, C	–1.5[(b)]
Strain hardening coefficient, K (MPa)	440[(a)]
Strain hardening exponent, n	0.42[(a)]

[(a)] Asad et al. (2014).
[(b)] Johnson and Holmquist (1989).

for creating a crack of unit area (Hillerborg et al., 1976) was implemented in the analysis. A linear material degradation process (path BC) was modeled based on the relation (ABAQUS/CAE, 2020)

$$D = \frac{l_c \overline{\varepsilon}^p}{2G_f} \overline{\sigma}_c \tag{3}$$

where l_c is a characteristic length that depends on the aspect ratio of the element sides, G_f is the fracture energy for creating a crack of unit area, and $\overline{\sigma}_c$ is the effective stress at the inception of material degradation, i.e., $\omega = 1$ (point B). The purpose for using l_c in Eq. (3) is to prevent an artificial decrease of the energy dissipation due to strain localization induced by the refinement of the FEM mesh. For a first-order, plane-strain element, l_c is set equal to the square root of the area of a finite element. Thus, an artificial decrease in energy dissipation was avoided by using an element aspect ratio close to unity and setting l_c equal to the square root of the area of the smallest finite elements. The degradation parameter D is defined by the relation $\overline{\sigma^*} = (1 - D)\overline{\sigma}$, where $\overline{\sigma^*}$ is the reduced effective stress due to the damage. A finite element is removed from the FEM model when $D = 1$. The value of G_f (Table 2) used in all simulations corresponds to 2024-T351 aluminum alloy.

2.3. Constitutive model

To model quasi-static, isothermal, isotropic strain hardening material behavior, the half-space is modelled to follow the constitutive stress-strain law (Johnson and Cook, 1985)

$$\overline{\sigma} = Y_0 + K\overline{\varepsilon}^n \tag{4}$$

where K is the strain hardening coefficient and n is the strain hardening exponent.

Yielding is determined by the von Mises yield criterion, given by

$$\overline{\sigma} = \left(\frac{3}{2} S_{ij} S_{ij}\right)^{1/2} = Y \tag{5}$$

where S_{ij} are components of the deviatoric stress tensor and Y is the current yield strength.

The evolution of plasticity is described by the equivalent plastic strain $\overline{\varepsilon}^p$, computed by

$$\overline{\varepsilon}^p = \int_\Omega \left(\frac{2}{3} d\varepsilon_{ij}^p d\varepsilon_{ij}^p\right)^{1/2} \tag{6}$$

where Ω is the strain path used to track the accumulation of plasticity and $d\varepsilon_{ij}^p$ are plastic strain increments.

2.4. Finite element simulations

All of the FEM simulations were performed in displacement-control mode using the multi-physics code ABAQUS/Explicit (ABAQUS/CAE, 2020). Special attention was given to the selection of the time step. A large time step in a quasi-static analysis that uses the explicit solver can yield significant dynamic effects, whereas a small time step can greatly increase the computation time. A mass scaling factor k_m was used in this study to reduce the computation time by $k_m^{1/2}$. To ensure that the selected time step preserves the quasi-static condition, the kinetic energy must be less than 5% of the internal energy. For the time step $\Delta t \approx 10$ ns used in all the simulations, the kinetic energy was found to be about 1% to 4% of the internal energy, which is within the admissible range.

2.5. Dimensionless parameters

To obtain generalized solutions, the input and output simulation parameters were normalized by appropriate quantities. Specifically, the dimensionless load $\overline{P}$ is defined by P/P_{Y_0}, where P_{Y_0} is the load at initial yield expressed by $P_{Y_0} = \pi R\left(p_0^2/E^*\right)$, where p_0 is the maximum Hertzian pressure at the inception of yielding given by $p_0 = 1.79Y_0$ (Mises yield criterion) and $E^* = E/\left(1 - \nu^2\right)$, where E and ν are the elastic modulus and Poisson's ratio, respectively. The dimensionless normal displacement (penetration depth) is defined by $\overline{d} = d/R$. The dimensionless plastic area is given by $\overline{A}_p = A_p/A_i$, where A_p is the plastic area, computed by summing up the areas of all the elements with $\overline{\varepsilon}^p > 0.002$, and A_i is the contact area established between the cylinder and the half-space before the commencement of oscillation, assuming a unit length distance in the out-of-plane direction. The dimensionless wear area $\overline{A}_w$ is obtained by dividing the wear area A_w, i.e., the sum of the areas of all the elements removed from the model ($D = 1$), by the plastic area A_p computed at the same instant of the simulation. The averaged fraction of the contact area in slip mode $\overline{A}_s$ is calculated before the removal of the fully damaged elements (i.e., $\omega < 1$) by dividing the total slip area by the total contact area, assuming a unit length distance in the out-of-plane direction, with both areas averaged over the same oscillation cycle.

3. Results and discussion

Insight into the progression of damage in an elastic-plastic half-space can be obtained by tracking the damage parameter ω during oscillation. Fig. 3 shows the evolution of ω in the first 5 oscillation cycles for $\overline{P} = 13$ and $\mu = 0.3$. Forward plastic shearing during the right stroke of the first cycle ($N = 1/4$) caused damage to the elements adjacent to the contact interface, surface sinking, and the formation of a shallow pile-up (Fig. 3(a)). Subsequent backward sliding of the cylinder up to the center of oscillation ($N = 1/2$) resulted in the lateral expansion of the damage zone and additional damage at the right oscillation edge ($x = +\delta$) due to more plastic deformation accumulated during the unloading (Fig. 3(b)). Backward plastic shearing during the left stroke of the first cycle ($N = 3/4$) enlarged the damage zone in the lateral direction, increased the material pile-up at the left oscillation edge ($x = -\delta$), and produced a pocket of excessive damage adjacent to the left oscillation edge (Fig. 3(c)), which extended slightly toward the oscillation center ($x = 0$) at the end of the first cycle ($N = 1$) (Fig. 3(d)). The asymmetric damage distribution showing more damage at the left oscillation edge is attributed to the larger volume of material plowed during backward sliding due to the increase of the penetration depth in the previous stage of forward sliding. The second cycle ($N = 2$) created a fairly uniform, highly intensified, enlarged damage zone extending deeper into the substrate owing to further advancement of the cylinder

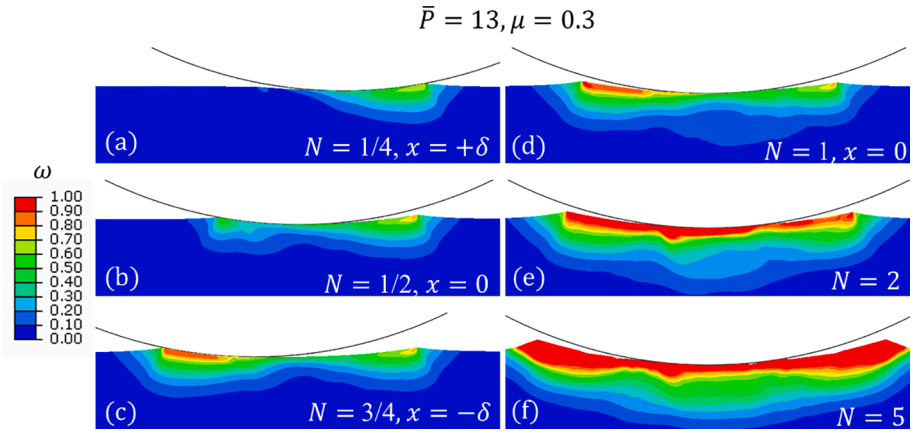

Fig. 3. Evolution of damage parameter ω during the (a-c) first oscillation cycle and after the (d) first, (e) second, and (f) fifth oscillation cycles.

into the half-space (Fig. 3(e)). The damage zone continued to expand in the following cycles due to the proliferation of plasticity, as shown by the damage contours obtained after 5 cycles ($N = 5$) (Fig. 3(f)). Repetitive forward and backward plastic shearing resulted in material build-up at both oscillation edges, larger pile-ups, and deeper penetration of the cylinder. Moreover, the removal of the fully damaged elements ($\omega = 1$) adjacent to the contact interface, when the degradation parameter D reached unity, also contributed to the increase of the penetration depth. As this process perpetuated itself during the oscillation, elements at deeper locations reaching full damage ($\omega = 1$) were also removed ($D = 1$), aiding the enlargement of both the damage zone and the pile-ups (Fig. 3(f)).

Fig. 4 shows the dimensionless normal displacement (penetration depth) $\bar{d}$ as a function of oscillation cycles N for $\bar{P} = 13 - 79$ and $\mu = 0.3$. As expected, the penetration depth increased with the load. Even though some of the simulations did not reach 10 oscillation cycles due to convergence problems, the obvious trend is for $\bar{d}$ to stabilize after a few cycles. This trend is more apparent in the high-load cases ($\bar{P} \geq 33$) showing a stable $\bar{d}$ after ~5 cycles. This behavior may be attributed to the greater conformity of the cylinder with the substrate at higher loads that intensified plastic shearing and fostered the formation of larger pile-ups.

The effects of the load and the coefficient of friction on the development of plasticity during oscillatory contact can be further interpreted in the light of the simulation results of the dimensionless plastic area $\bar{A}_p$ shown in Fig. 5. (The fewer oscillation cycles attained in some of the simulations are due to convergence problems instigated by the excessive deformation of some elements.) All of the simulations show a sharp increase of $\bar{A}_p$ after a few cycles. The results also show that the lower the load and the higher the coefficient of friction, the more cycles for $\bar{A}_p$ to stabilize. Conversely to the sharp increase of A_p with the load (data not

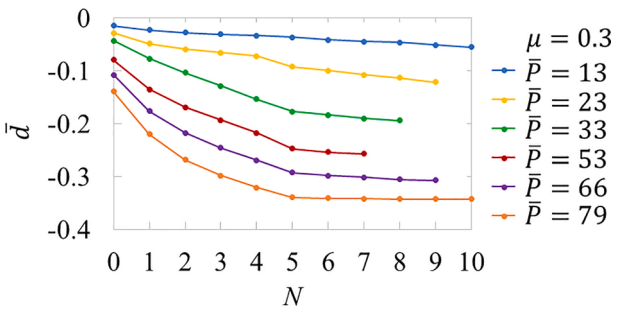

Fig. 4. Dimensionless penetration depth $\bar{d}$ versus number of oscillation cycles N for $\bar{P} = 13 - 79$ and $\mu = 0.3$.

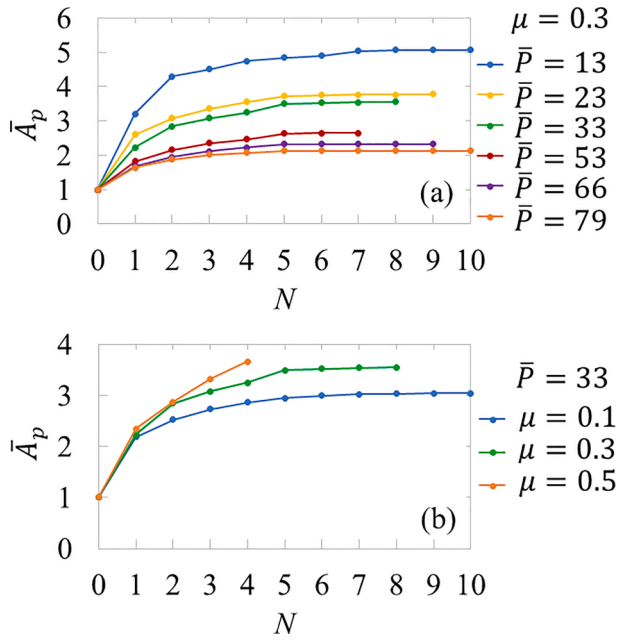

Fig. 5. Dimensionless plastic area $\bar{A}_p$ versus number of cycles N for (a) $\bar{P} = 13 - 79$ and $\mu = 0.3$ and (b) $\mu = 0.1 - 0.3$ and $\bar{P} = 33$.

shown here for brevity), $\bar{A}_p$ decreased with the increase of the load (Fig. 5(a)), indicating the development of more plastic deformation during the loading phase than the oscillation phase of the high-load simulations. This does not imply that a low load produces a larger plastic area A_p (for a given number of cycles), but a more prominent effect of the shear surface traction due to sliding in the oscillation phase of the low-load simulations. For instance, after 10 cycles, the plastic zone for $\bar{P} = 13$ increased by a factor of ~5 compared to a factor of ~2 for $\bar{P} = 79$. Furthermore, the increase of $\bar{A}_p$ with μ at a given load (Fig. 5(b)) demonstrates an increasing contribution of the shear surface traction to plasticity with increasing friction. The increase of friction augmented plastic shearing in the subsurface, dramatically increasing $\bar{A}_p$ after a few cycles. For example, for a fixed load ($\bar{P} = 33$), the plastic zone size in the high-friction simulation ($\mu = 0.5$) increased by a factor of >3.5 after only 4 cycles, as opposed to a factor of <3 in the low-friction simulation ($\mu = 0.1$).

Important insight into the development of plasticity with the accumulation of oscillation cycles leading to the loss of material was obtained by tracking the dimensionless damage parameter ω during the evolution of damage in the plastically deformed elements . The increase

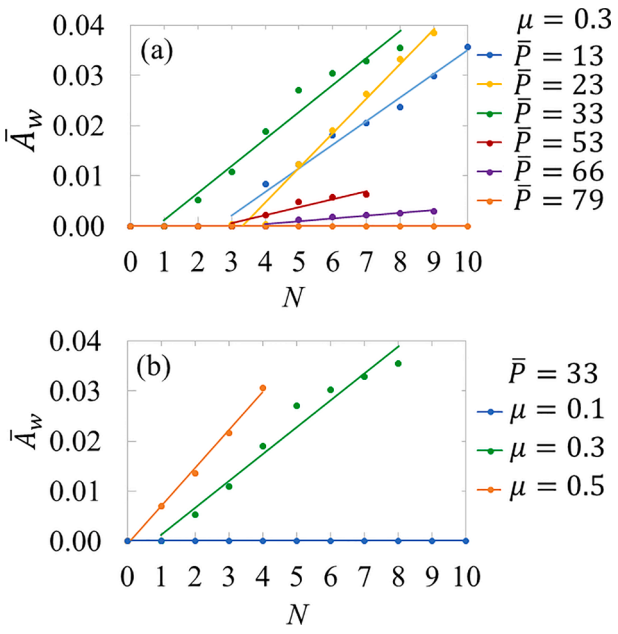

Fig. 6. Dimensionless wear area $\bar{A}_w$ versus number of oscillation cycles N for (a) $\bar{P} = 13 - 79$ and $\mu = 0.3$ and (b) $\mu = 0.1 - 0.3$ and $\bar{P} = 33$.

of ω can be linked to the progression of damage. When $\omega = 1$ ($D = 0$) in a certain element, it is presumed that the element enters the material degradation regime where it undergoes a stiffness reduction, resulting in the decrease of its load carrying capacity (Fig. 2) and, ultimately, its removal from the model when full degradation is reached ($D = 1$). Fig. 6(a) shows the variation of $\bar{A}_w$ with the number of oscillation cycles N for $\mu = 0.3$ and $\bar{P} = 13 - 79$. All of the simulations demonstrate a fairly linear increase of $\bar{A}_w$ with N, consistent with the linear variation of the wear volume with the sliding distance predicted by Archard's wear law. Fig. 6(b) shows the effect of the coefficient of friction μ on the evolution of $\bar{A}_w$ for $\bar{P} = 33$. The marginal plastic shearing in the low-friction simulation ($\mu = 0.1$) did not cause any loss of material. However, the increase of the coefficient of friction intensified plastic shearing, yielding a fairly linear increase of $\bar{A}_w$ with N, much faster in the high-friction simulation ($\mu = 0.5$) than the intermediate-friction simulation ($\mu = 0.3$).

Furthermore, Fig. 6(a) shows an increasing trend of the wear area with the load increase up to $\bar{P} = 33$, which is also consistent with Archard's wear law. However, an opposite trend is shown for higher loads ($\bar{P} \geq 53$). This seemingly counterintuitive behavior can be explained by considering *iso*-strain contour distributions of the plastic shear strain γ^p_{xy} representative of low-load ($\bar{P} = 13$) and high-load ($\bar{P} = 79$) oscillatory contacts, corresponding to the linear increase of wear with accumulating cycles and no wear, respectively (Fig. 6(a)). For low-load oscillatory contact, γ^p_{xy} is confined at the oscillation edges after the first cycle, with the left zone of γ^p_{xy} demonstrating slightly higher plastic strains (Fig. 7(a)), a consequence of the asymmetric nature of the shearing process. The second cycle increased the deformation in the two plastic shear zones (especially the right zone), enlarged the material pile-ups at the oscillation edges, and further increased the penetration of the cylinder into the half-space (Fig. 7(c)). A similar, though less pronounced, tendency was encountered after the third cycle, with the highest γ^p_{xy} arising at the contact interface (Fig. 7(e)). Thus, in the low-load simulation, the region showing the highest propensity for material loss is adjacent to the contact interface, where plastic shearing is more prominent. For high-load oscillatory contact, however, the *iso*-strain contours of γ^p_{xy} reveal a different deformation behavior. Specifically, while plastic shearing is again confined at the oscillation edges after the first cycle (Fig. 7(b)), the plastic shear zones are located well below the contact interface and the strains are smaller than those in the low-load simulation (Fig. 7(a)). (Note the use of different magnifications in the low- and high-load simulation results shown in Fig. 7 to better reveal the regions of high γ^p_{xy} strain.) This difference is attributed to the significantly larger volume of material resisting the oscillatory motion of the cylinder for $\bar{P} = 79$ than $\bar{P} = 13$, as evidenced by the results of the penetration depth (Fig. 4). Similar to the low-load simulation, the penetration depth and the size of the plastic shear zones increased in the second (Fig. 7(d)) and third (Fig. 7(f)) cycles of the high-load simulation; however, the maximum γ^p_{xy} is located away from the contact interface and its magnitude is less than that in the low-load simulation. As a result, less plastic shearing occurred in the high-load simulation due to less slip at the contact interface, a consequence of the reduced lateral movement instigated by the larger volume of material surrounding the deeper penetrating cylinder. This mitigated the conducive effect of friction on plastic shearing, consequently suppressing the build-up of plasticity-induced damage and, in turn, weakening the propensity for wear.

Additional insight into the reduced interfacial slip in high-load oscillatory contacts can be obtained by inspecting the effect of the applied load on the amount of slip at the contact interface. Fig. 8 shows the averaged fraction of the contact area in slip mode $\bar{A}_s$, calculated before the instigation of material loss (i.e., $\omega < 1$) as a function of load $\bar{P}$ for $\mu = 0.3$. The decreasing tendency of $\bar{A}_s$ with increasing $\bar{P}$ confirms the decrease of the interfacial slip with the load increase. In particular, $\bar{A}_s$ is greater than 30% in the low-load range ($\bar{P} < 20$) and less than 15% in the high-load range ($\bar{P} > 60$). The results shown in Fig. 8 provide

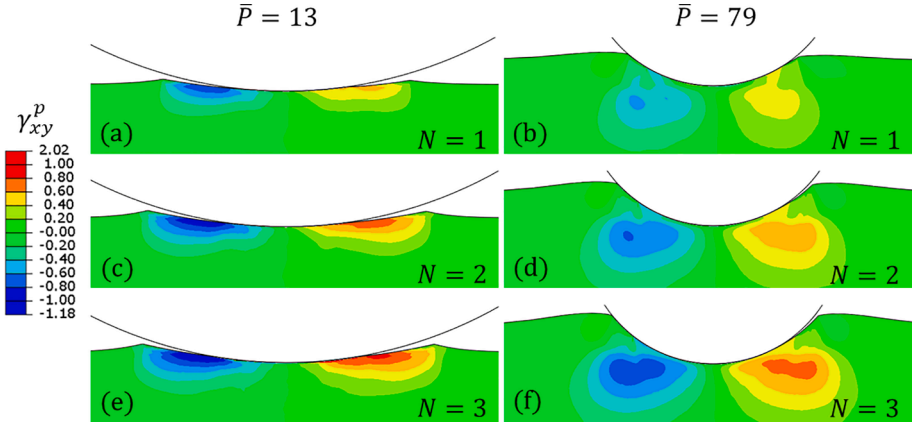

Fig. 7. Contours of plastic shear strain γ^p_{xy} after the first ($N = 1$), second ($N = 2$), and third ($N = 3$) oscillation cycles for $\bar{P} = 13$ (left column), $\bar{P} = 79$ (right column), and $\mu = 0.3$.

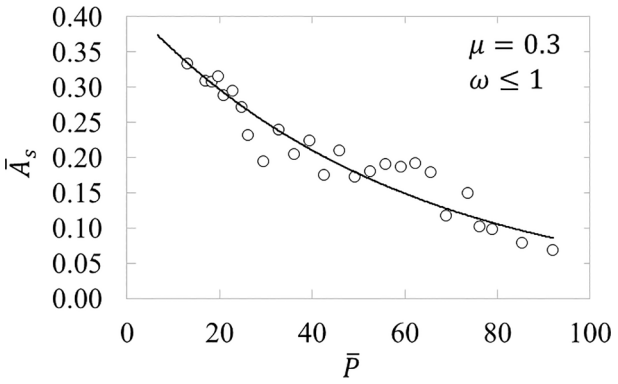

Fig. 8. Averaged fraction of the contact area in slip mode $\bar{A}_s$ before the instigation of the removal of fully damaged elements versus load $\bar{P}$ for $\mu = 0.3$.

additional support to the decreasing intensity of plastic shearing (henceforth, less damage accumulation and lower propensity for material loss) with the increase of the applied load.

The present analysis provides a mechanistic understanding of the synergistic effects of load and friction on plasticity-induced damage leading to progressive material degradation and, ultimately, the loss of material in oscillatory contacts. The quasi-static, isothermal, strain hardening constitutive model used in this study can be modified to account for strain rate and temperature effects on plasticity-induced damage by implementing the full ductile failure criterion of Johnson and Cook (1985) and a multi-scale roughness description by superimposing a fractal surface profile to the cylinder's contour to create a fractal-regular surface (Wang and Komvopoulos, 1994). From a fundamental standpoint, this study provides a computational framework for performing parametric studies of the mechanical performance of oscillatory contacts operating under various loading and friction conditions.

4. Conclusions

A contact mechanics analysis of the evolution of plasticity in oscillatory contacts was performed to examine how the accumulation of plasticity-induced damage and material degradation lead to the removal of material. A damage model based on a ductile failure criterion was used to simulate the loss of material by removing the fully damaged elements from the model. A parametric FEM study was conducted to elucidate the effects of the applied load and coefficient of friction on the advancement of plasticity and the loss of material in terms of representative dimensionless parameters. The main findings of the present study can be summarized as following.

(1) A dimensionless damage parameter ω was used to track the progression of plasticity-induced damage that leads to the loss of material in oscillatory contacts for a range of the load and the coefficient of friction.
(2) The penetration depth increased with the load and the number of oscillation cycles, showing a clear trend to stabilize after a few cycles, which was more evident in the high-load simulations.
(3) The dimensionless plastic and wear areas increased with the coefficient of friction due to the intensification of plastic shearing, revealing the critical role of friction in the development of plasticity, the advancement of damage, and the instigation of material loss.
(4) The dimensionless wear area increased linearly with the oscillation cycles and the load up to a threshold, consistent with Archard's classical theory of adhesive wear. However, an opposite trend was observed with loads above the load threshold, which was explained by considering the distribution of the plastic shear strain in the low- and high-load oscillations and the load dependence of the averaged fraction of contact area in slip mode. While the highest plastic shear strains arose adjacent to the contact interface in the low-load oscillations, their locations shifted well below the contact interface and their magnitudes decreased in the high-load oscillations.
(5) The averaged fraction of the contact area in slip mode demonstrated an overall tendency to decrease with the increase of the load, indicating a significant decrease in interfacial slip at high loads, which was attributed to the restricted movement of the cylinder due to the larger volume of the surrounding material. Consequently, less plastic shearing occurred in the high-load oscillations, resulting in less damage accumulation and loss of material.

The results of this study provide insight into the effects of the load and the coefficient of friction on the loss of material in oscillatory contacts due to the accumulation of plasticity. An important contribution of this work is the development of a computational methodology for performing mechanistic analyses of the effects of other important parameters, such as strain rate, temperature, surface roughness, and oscillation amplitude, on the evolution of plasticity-induced damage and the loss of material in oscillatory contacts.

Declaration of Competing Interest

The authors declare that they have no known competing financial interests or personal relationships that could have appeared to influence the work reported in this paper.

Data availability

Data will be made available on request.

References

ABAQUS/CAE, 2020. User's manual. Dassault Systèmes Simulia Corp., Providence, RI, USA.
Aghababaei, R., Warner, D.H., Molinari, J.-F., 2017. On the debris-level origins of adhesive wear. Proc. Natl. Acad. Sci. USA 114, 7935–7940.
Ambrico, J.M., Begley, M.R., 2000. Plasticity in fretting contact. J. Mech. Phys. Solids 48, 2391–2417.
Archard, J.F., 1953. Contact and rubbing of flat surfaces. J. Appl. Phys. 24, 981–988.
Asad, M., Mabrouki, T., Ijaz, H., Aurangzeb Khan, M., Saleem, W., 2014. On the turning modeling and simulation: 2D and 3D FEM approaches. Mech. Ind. 15, 427–434.
Ben Tkaya, M., Zahouani, H., Mezlini, S., Kapsa, Ph., Zidi, M., Dogui, A., 2007. The effect of damage in the numerical simulation of a scratch test. Wear 263, 1533–1539.
Björklund, S., 1997. A random model for micro-slip between nominally flat surfaces. ASME J. Tribol. 119, 726–732.
Block, J.M., Keer, L.M., 2008. Periodic contact problems in plane elasticity. J. Mech. Mater. Struct. 3, 1207–1237.
Cattaneo, C., 1938. Sul contato di due corpo elastici. Atti Accad. Naz. Lincei, Cl. Sci. Fis., Mat. Nat., Rend., 27, 342–348, 434–436, 474–478.
Chen, Z., Etsion, I., 2019. Model for the static friction coefficient in a full stick elastic-plastic coated spherical contact. Friction 7, 613–624.
Dimaki, A.V., Shilko, E.V., Dudkin, I.V., Psakhie, S.G., Popov, V.L., 2020. Role of adhesion stress in controlling transition between plastic, grinding and breakaway regimes of adhesive wear. Sci. Rep. 10, 1585.
Elwasli, F., Zemzemi, F., Mkaddem, A., Mzali, S., Mezlini, S., 2015. A 3D multi-scratch test model for characterizing material removal regimes in 5083-Al alloy. Mater. Des. 87, 352–362.
Eriten, M., Polycarpou, A.A., Bergman, L.A., 2011. Physics-based modeling for fretting behavior of nominally flat rough surfaces. Int. J. Solids Struct. 48, 1436–1450.
Etsion, I., 2010. Revisiting the Cattaneo-Mindlin concept of interfacial slip in tangentially loaded compliant bodies. ASME J. Tribol. 132, 020801.
Fouvry, S., Kapsa, P., Vincent, L., 1996. Quantification of fretting damage. Wear 200, 186–205.
Frérot, L., Aghababaei, R., Molinari, J.-F., 2018. A mechanistic understanding of the wear coefficient: From single to multiple asperities contact. J. Mech. Phys. Solids 114, 172–184.

Giannakopoulos, A.E., Suresh, S., 1998. A three-dimensional analysis of fretting fatigue. Acta Mater. 46, 177–192.
Goryachev, I.G., Malanchuk, N.I., Martynyak, R.M., 2012. Contact interaction of bodies with a periodic relief during partial slip. J. Appl. Math. Mech. 76, 621–630.
Hertz, H., 1882. Über die berührung fester elastischer körper (On the contact of rigid elastic solids). J. Reine Angewandte Mathematik 92, 156–171. (English translation: Hertz, H. (1896). On the contact of elastic solids. In: Miscellaneous Papers by H. Hertz. Jones, D.E., and Schott, G.A. (eds.), London: Macmillan, pp. 146–162.).
Hillerborg, A., Modëer, M., Petersson, P.-E., 1976. Analysis of crack formation and crack growth in concrete by means of fracture mechanics and finite elements. Cem. Conc. Res. 6, 773–781.
Jäger, J., 1998. A new principle in contact mechanics. ASME J. Tribol. 120, 677–684.
Johnson, G.R., Cook, W.H., 1985. Fracture characteristics of three metals subjected to various strains, strain rates, temperatures and pressures. Eng. Fract. Mech. 21, 31–48.
Johnson, G.R., Holmquist, T.J., 1989. Test data and computational strength and fracture model constants for 23 materials subjected to large strains, high strain rates, and high temperatures. Tech. Rep. LA-11463-MS, Los Alamos National Laboratory.
Klimchuk, T., Ostryk, V., 2020. Stress distributions in the Cattaneo-Mindlin problem on a contact with slip and adhesion of two cylindrical bodies. Front. Mech. Eng. 6, 22.
Kuno, M., Waterhouse, R.B., Nowell, D., Hills, D.A., 1989. Initiation and growth of fretting fatigue cracks in the partial slip regime. Fatigue Fract. Eng. Mater. Struct. 12, 387–398.
Lou, Y., Yoon, J.W., Huh, H., 2014. Modeling of shear ductile fracture considering a changeable cut-off value for stress triaxiality. Int. J. Plast. 54, 56–80.
Mindlin, R.D., 1949. Compliance of elastic bodies in contact. ASME J. Appl. Mech. 16, 259–268.
Mindlin, R.D., Deresiewicz, H., 1953. Elastic spheres in contact under varying oblique forces. ASME J. Appl. Mech. 20, 327–344.
Mostaani, A., Pereira, M.P., Rolfe, B.F., 2015. Comparison of ductile damage models during scratch tests – A numerical study. Proc. 8th Int. Conf. BALTTRIB'2015, 26-27 Nov. 2015, pp. 126-133.
Pereira, K., Yue, T., Abdel Wahab, M., 2017. Multiscale analysis of the effect of roughness on fretting wear. Tribol. Int. 110, 222–231.
Salib, J., Kligerman, Y., Etsion, I., 2008. A model for potential adhesive wear particle at sliding inception of a spherical contact. Tribol. Lett. 30, 225–233.
Song, Z., Komvopoulos, K., 2014. Contact mechanics analysis of oscillatory sliding of a rigid fractal surface against an elastic–plastic half-space. Philo. Mag. 94, 3215–3233.
Wang, S., Khatir, S., Abdel Wahab, M., 2020. Proper orthogonal decomposition for the prediction of fretting wear characteristics. Tribol. Int. 152, 106545.
Wang, S., Komvopoulos, K., 1994. A fractal theory of the interfacial temperature distribution in the slow sliding regime: Part II–Multiple domains, elastoplastic contacts and applications. ASME J. Tribol. 116, 824–832.
Yue, T., Abdel Wahab, M., 2017. Finite element analysis of fretting wear under variable coefficient of friction and different contact regimes. Tribol. Int. 107, 274–282.
Zhang, H., Etsion, I., 2021. Evolution of adhesive wear and friction in elastic-plastic spherical contact. Wear 478–479, 203915.